UC Berkeley
UC Berkeley Previously Published Works

Title
Laser Ablation Molecular Isotopic Spectrometry for Molecules Formation Chemistry in Femtosecond-Laser Ablated Plasmas

Permalink
https://escholarship.org/uc/item/55q783xd

Journal
Analytical Chemistry, 89(14)

ISSN
0003-2700

Authors
Hou, Huaming
Mao, Xianglei
Zorba, Vassilia
et al.

Publication Date
2017-07-18

DOI
10.1021/acs.analchem.7b01750

Peer reviewed

Laser Ablation Molecular Isotopic Spectrometry for Molecules Formation

Chemistry in fs-Laser Ablated Plasmas

Huaming Hou,[†, ‡] Xianglei Mao[*, ‡] Vassilia Zorba,[‡] Richard E. Russo[‡, §]

[†]The Peac Institute of Multiscale Sciences, Chengdu, Sichuan 610031, People's Republic of China

[‡]Lawrence Berkeley National Laboratory, Berkeley, California 94720, United States

[§]Applied Spectra, Inc., Fremont, CA 94538, USA

ABSTRACT Recently, laser ablated molecular isotopic spectrometry (LAMIS) has expanded its capability to explore molecules formation mechanism in laser induced plasma in addition to isotope analysis. LAMIS is powerful tool for tracking the origination of atoms that involved in formation of investigated molecules by labeling atoms with its isotopic substitution. The evolutionary formation pathways of organic molecules, especially of C_2 dimers and CN radicals, were frequently reported. However, very little is known about the formation pathways for metallic radicals and heterodimers in laser ablated plasma. This research focuses on elucidating the formation pathways of AlO radicals in femtosecond laser ablated plasma from ^{18}O-labeled Al_2O_3 pellet. Plasmas expanding with strong forward bias in the direction normal to the sample surface were generated in the wake of weakly ionized channel created by femtosecond laser. The formation mechanism of AlO and influence of air were investigated with multiple plasma diagnostic methods such as monochromatic fast gating imaging, spatiotemporal resolved optical emission spectroscopy and LAMIS. An advanced LAMIS fitting procedure was used to deduce the spatiotemporal distributions of $Al^{18}O$ and $Al^{16}O$ number densities and also their ratios. We found that $Al^{16}O/Al^{18}O$ number density ratio is higher for plasma portion closer to the sample surface, which suggests that chemical reactions between plasma plume and ambient air are more intense at the tail of plasma. The results also reveals that direct association of free Al and O atoms is the main mechanism for the formation of AlO at early stage of plasma. To the contrast, chemical reactions between plasma materials and ambient oxygen molecules, and isotope exchange effect are the dominate mechanisms of the formation of AlO and evolution of $Al^{16}O/Al^{18}O$ number density ratio at late stage of plasma.

Introduction

Laser-induced breakdown spectroscopy (LIBS) has been advanced as a versatile analytical technique over past several decades because it has shown efficient and promising results in the field of elemental analysis, even at standoff distance.[1–3] The laser sampled materials undergoes vaporization, atomization, ionization and recombination in the plasma plume, and the excited atomic, ionic, molecular species emit at their characteristic wavelength.[4,5] Recently, the importance of analyzing molecular emissions in laser ablated plasmas has been raised drastically for the purpose of recognition of organic compounds,[6–9] detection of halogen elements[10] and quantitative analysis of isotopes.[11–16] The molecular emission is tightly related to the structural and chemical-physical properties of molecules, together with experimental parameters.[17] Factors altering the electron distribution within the organic molecules have been reported to have a direct impact on its ensuing optical emissions, because electron structure governs the breakage of molecular bonds and further determines the extent of atomization and fragmentation of laser sampled materials.[17] The acquired molecular emission spectra are relevant to complex plasma processes such as photochemistry, association of atoms into a molecule, dissociation of fragments and combustion of atomized species, and vary significantly in space and time.[17–19] The study of chemical reaction pathways and formation mechanism of molecules is essentially important whilst seeking chemical information of samples through molecular emission from plasma.

Spatiotemporal behaviors of molecular emission and elucidations of molecules formation routes have been investigated in several works.[20–22] However, most of these works are limited on establishing direct link between plasma emission and molecular structure, or origination of atoms that form molecules. For example, it is hard to differentiate the origination of N and O atoms in case of laser ablation of compounds with N and O elements in air. The development of laser ablation molecular isotopic spectrometry (LAMIS) provides a versatile technique for the study of molecules formation mechanism because it is powerful to track the origination of atoms that involved in formation of investigated molecules by labeling atoms with its isotopic substitution.[13,23–25] An investigation of ns-laser ablation of ^{13}C-labeled benzoic reveals that direct release of fragments from molecules acts as

a complementary mechanism for the formation of C_2 molecules and CN formation likely involves atomic carbon or species with a single carbon atom.[23] Similar study of fs-laser ablation of urea and deuterated urea $-CO(ND_2)_2-$ also reveals that direct release of native molecular bonds is a significant source that populates plasma with NH radicals.[25] The molecular emission also was found to be related to the surrounding environment, rather than solely connected with ablated material stoichiometry.[17] The contribution of fragmentation to the apparent spectra depends on the type of atmospheric gas as a result of interaction between ablated materials and ambient gases.[24] In addition, the contributions of association of free atoms and fragmentation mechanism to the formation of molecules differ at different portions or evolution times of plasma,[23,24] and the laser induced shockwave can also mediate the formation of molecules.[19] Thus, the formation of molecules in plasma is rather complex. Despite these interesting findings, most of the studies are focused on the formation of non-metallic dimers or radicals. Metallic radicals and heterodimers can also form in plasma and play critical role in isotopic analysis with LAMIS technique and other spectrometric method.[26,27] However, the kinetics of metallic molecules formation and its relation to plasma chemistry are seldom investigated and not well-known.[19]

The AlO blue-green system has a relative large transition probability, and was extensively studied due to its importance in astrophysics.[28,29] The emission spectrum of AlO from laser induced plasma was also widely investigated for the purposes of plasma diagnostics.[18] Precisely AlO spectrum simulations enabled that AlO spectrum emitted from laser induced plasma can be well fitted with theoretical model,[30–33] and provide a new method of predicting chemical reactions leading to the formation of AlO radicals.[32] Simultaneously analyzing the spectra of molecular isotopologues shows great advantage in seeking insights related to formation mechanism of molecules in plasma chemistry, and AlO is a good candidate because of large isotope shifts of band spectra of $Al^{16}O$ and $Al^{18}O$ radicals.

The fs-laser ablation shows outstanding advantage in formation of molecules in plasma plumes over ns-laser ablation,[34–36] which motivated growing investigations. Compared to ns-laser ablation, fs-laser ablation is absent of laser-plasma interaction, and the produced plasma typically features lower temperature,[37] which favors the formation of molecules. As a result, spectra resulting from ns-laser

ablation mainly manifested atomic signals, whereas emissions from fs-laser ablated plasma are more likely dominated by molecular bands.[36,38] Moreover, fs-laser produced plasma features narrower angular distributions in plasma expansion,[39] which suggests a lower plasma-atmosphere interaction.[34,40] In addition, emission spectra acquired with fs-laser ablated plasma exhibit a lower continuum emission background and narrower line broadening,[39] which favors the molecular band analyzing. Hence, the fs-laser ablation regime together with LAMIS technique provides a versatile method for understanding the formation routes of molecules.

This study focused on the formation mechanism of metallic heterodimers in fs-laser induced plasma in air. Formation routes of AlO molecules were investigated, and Al_2O_3 pellet samples labeled by ^{18}O were used to differentiate the oxygen from air. Plasmas expanding with strong forward bias in the direction normal to the sample surface were ablated in the wake of weakly ionized air channel created by femtosecond laser. Multiple diagnostics methods, viz. monochromatic fast gating imaging, spatiotemporal resolved optical emission spectroscopy and LAMIS, were used to infer plasma chemistry on AlO formation throughout the evolution of the laser ablated plasma. Several reactions involving association of Al and O atoms into a molecule, combusting of Al species with surrounding oxidizers and isotopic oxygen exchange has been raised and discussed.

DESCRIPTION OF THE MEASUREMENT SETUP

Optical Setup. A Ti:Sapphire laser, operating at 800 nm, with 35 fs pulse duration and 5 mJ pulse energy, was used. The laser pulse was focused with a fused-silica lens (f=15 cm). The geometrical focus was about 1.8 mm down to the sample surface, likely caused by the self-focusing effect and filamentation phenomenon, the fs-laser beam was focused above sample surface and a short weakly ionized air plasma channel was created. Laser energy was coupled onto sample surface and plasmas were produced. The spot diameter is about 0.2 mm and laser fluence was 16 J /cm^2. The plasma was directly imaged by two lens (Φ=2 inches) onto the entrance slit of Czerny-Turner spectrograph (Horiba JY 1250M, 2400 g/mm) configured with an intensified CCD (Priceton Instruments, PI-MAX). The emission of plasma was acquired in two different configurations. (1) For temporally resolved plasma image measurements, the spectrograph grating operated in reflection

mode (0 order) and the entrance slit was fully opened (3 mm). A band pass filter was placed in front of the spectrograph entrance slit to detect the AlO emission. The imaging system was well aligned to get a clear image of AlO B→X ($\Delta v = 0$) band emission with spatial resolution about 40 lp/mm. (2) For spatiotemporally resolved spectra measurements, the entrance slit was 50 μm, and the AlO B→X ($\Delta v = -1$) molecular bands were recorded. The spectral resolution of the spectrograph system was about 15 pm.

Sample. To differentiate the oxygen in air, ^{18}O-enriched Al_2O_3 (Sigma-Aldrich, 95 atom % ^{18}O) was used as the sample. The powder samples were pressed with 7 tons of force for 4 min into a one-centimeter pellet.

Data Acquisition. A single measurement of image or spectrum comprises plasmas from 20 laser pulses, respectively. To record the temporal evolution of plasma emission, a delayed detection window with increasing gate width was used to compensate for the decreasing plasma emission intensity. The sample was ablated with 20 laser shots per sampling location. The magnification of plasma image on ICCD pixels was calibrated with reticles, and each ICCD pixel row corresponded to 6 μm height in the plasma. The dark current of the detector was recorded and all presented spectra were dark current subtracted. Flatfield correction for ICCD was also performed.

Binning. As stated above, the ICCD was set to acquire spectra with image mode. Several sub-regions of the two-dimensional CCD array were averaged afterwards. Tests showed that averaging of 50 pixels (correspond to 300 μm, 6 μm/pixel row) for each sub-region give good signal-to-noise ratio whilst maintaining sufficient number of regions so that the plasma can be well spatially resolved.

RESULTS AND DISCUSSION

Plume Hydrodynamics: AlO imaging Plasma emission spectrometry is typically used to gauge the distributions of excited species in laser ablated plumes and evaluate the plasma properties. Measurement of the spatiotemporal behavior of molecules and emission spectra is helpful to understand the distribution of different excited species in plasma plume. Both sample materials and air molecules contribute oxygen atom to the formation of AlO molecules. LAMIS technique in conjunction with fast photography provides the spatiotemporal evolution of isotopic species in the

plume, and this information is extremely usefully for understanding the laser ablation plume chemical reactions and formation mechanism of molecules.

Figure 1(a-h) shows eight time-resolved plasma emission images. A 10 nm FWHM bandpass filter centered at 488 nm was used for plasma image measurements. The filter only allows the transmissions of AlO $\Delta v = 0$ bands of $B\,^2\Sigma^+ \to X\,^2\Sigma^+$ system, and no significant continuum emission contributes to the spectra acquired after 0.5 μs, according to the spectra recorded by spectrograph. Thus the images taken after 0.5 μs represent the distribution of AlO species in the plume. The plasma is found to propagate normal to the sample surface. The maximum plasma propagation distance can be up to 4 mm, whereas the plasma maintains similar width, ~ 0.4 mm. The expansion of plasma from Al_2O_3 sample is limited inside the region of weakly ionized air plasma channel （c.f. Fig.1）. The emission persistent time of the air plasma is less than 10 ns. For this experiment, a fs-laser pulse with 35 fs duration and 5 mJ energy was employed to produce strong plasma, the power is over the critical power for self-focusing.[41] The abnormal plasma evolution is the consequence of the nonlinear propagation of fs-laser beams and related nonlinear phenomenon such as filamentation, creation of vortices,[42] pre-excitation of air molecules above ablation area before producing plasma. Basically, a long-lived underdense channel was created above the laser radiation spot, which modifies the propagation of laser induced plasma. A full discussion of the plasma interact with the air affected by fs-laser through nonlinear effect is beyond the scope here and will be address in another paper.

Re-construction of Molecular Components via Fitting Procedure The rotational and vibrational energy levels of diatomic molecules are directly related to the reduced mass of two atoms. The energy levels are changed upon replacement of an atom by its isotopes. As a result, the molecular spectral structure shifts and the isotopic shifts allow the origination analysis of oxygen in formed AlO isotopologue molecules. The molecular bands of AlO are red-degraded, and the $B\,^2\Sigma^+ \to X\,^2\Sigma^+$ transition dominates the emission of AlO in plasma. Electronic transition involving a change in large Δv (i.e., when $v' \neq v''$) results in larger isotopic shifts. The AlO $\Delta v = -1$ bands of $B\,^2\Sigma^+ \to X\,^2\Sigma^+$ system were chosen in this study because of its strong intensity and appreciable isotopic shifts. Compared to our previously reported algorithm for isotopologue molecular bands synthetization,[12,16,23,43] three

modifications were implemented to improve the synthetic spectra. First, the theoretical spectra for $Al^{18}O$ and $Al^{16}O$ were synthetized based on the database from Patrascu *et al.*[44] instead of calculation using the reported molecular spectroscopic constants.[18,45] The database is deduced by a combination of empirical and *ab initio* method, and provides more accurate wavelength positions for rotational bands with high J numbers, especially for $Al^{18}O$. Second, three vibrational bands ((0,1), (1,2) and (2,3))were used to construct the synthetic spectra, which consists three $\Delta v = -1$ bands of AlO. Previously reported LAMIS works mostly utilized only one single band (i.e. C_2 d $^3\Pi_g \rightarrow$ a $^3\Pi_g$ (1–0) band, BO A $^2\Pi_i \rightarrow$ X $^2\Sigma^+$ (0–2) band, CN B $^2\Sigma^+ \rightarrow$ X $^2\Sigma^+$ (0–1)) for isotopic analysis.[13] Third, the tails of $\Delta v = 0$ bands enter the $\Delta v = -1$ spectral region, which can interference the $\Delta v = -1$ bands. A synthetic spectra including $\Delta v = 0$ bands could indeed improve the overall accuracy.[14]

Isotope information was extracted by fitting the experimental spectra with synthetic molecular spectra. The fitting approach was similar to our previously reports.[16,26] Briefly, a set of spectra for $Al^{16}O$ and $Al^{18}O$ (denoted as $I_{Al^{16}O}^{syn}(\lambda, T)$ and $I_{Al^{18}O}^{syn}(\lambda, T)$) were generated for each rotational component in the AlO $B^2\Sigma^+ \rightarrow X^2\Sigma^+$ (0,0), (1,1), (2,2), (0,1), (1,2) and (2,3) bands. Intensity distribution of each rotational/vibrational component was assigned based on the rotational/vibrational line strength and the Boltzmann distribution under temperature T, assuming the rotational temperature and vibrational temperature are the same. The synthetic spectral band of $Al^{16}O$ can be expressed as:

$$I_{Al^{16}O}^{syn}(\lambda, T) = I_{Al^{16}O\ (0,0)}^{syn}(\lambda, T) + I_{Al^{16}O\ (1,1)}^{syn}(\lambda, T) + I_{Al^{16}O\ (2,2)}^{syn}(\lambda, T) + I_{Al^{16}O\ (0,1)}^{syn}(\lambda, T) +$$

$$I_{Al^{16}O\ (1,2)}^{syn}(\lambda, T) + I_{Al^{16}O\ (2,3)}^{syn}(\lambda, T) \tag{1}$$

The synthetic spectra for $Al^{16}O$ together with $Al^{18}O$ take the following form:

$$I_{AlO}^{syn} = \left[\alpha \times I_{Al^{18}O}^{syn}(\lambda, T) + \beta \times I_{Al^{16}O}^{syn}(\lambda, T) \right] \tag{2}$$

The ratio of coefficients $R = \alpha / \beta$ corresponds to the isotopic ratio. Notice that α, β are proportional to the number of AlO molecules, other than the bandhead intensity. The influence of temperature on apparent molecular band intensity was compensated in our simulation. The same fitting algorithm as previously reported was used,[16] which located the best combination of all fitting parameters by minimization the sum of the squares of the fitting residuals $[\epsilon(\lambda)]$ at all wavelengths of the experimental spectrum, I_{AlO}^{expt}, through:

$$I_{AlO}^{expt} = I_{AlO}^{syn} + I_{continuum} + \epsilon(\lambda) \tag{3}$$

The fitting quality is gauged by relative residual, which is defined as:

$$Res = \sqrt{\sum \left(\frac{I^{exp} - I^{syn}}{I_{max}^{exp} - I_{continuum}} \right)^2 \Big/ N} \tag{4}$$

N is the number of wavelength data point.

Figure 2 shows a typical LAMIS spectrum acquired from the $Al^{18}O$-enriched Al_2O_3 pellet and its fitting. The experimental spectrum and fitted spectrum matches well regarding to the rotational structures and intensities of each rotational and vibrational band, and the fitting procedure returns the ratio $^{18}O/^{16}O = 0.7$ and $T_{rot} = 3386$ K. Rotational lines in the bands were deconvolved. It is noticeable that the contribution of the rotational tails of $\Delta v = 0$ band to $Al^{16}O$ (0,1) bandhead intensity is ignorable. However, the interference will be clearly observed whilst the $^{18}O/^{16}O$ ratio is low and plasma temperature is high, as demonstrated by Bol'shakov et al.[13] The intensities of AlO (0,0) band rotational lines with high J-numbers would be stronger at higher plasma temperature conditions, which would bring more interference to the apparent structures of AlO $\Delta v = -1$ bands. From this point of view, the fs-laser shows advantage over ns-laser for LAMIS analysis because fs-laser typically produces plasma with much lower temperature.[18] Only at very early time, the rotational temperature of fs-laser ablated plasma can be over 4000 K for this experiment, as will be addressed below.

Temporal Evolution of The AlO Emission From The Plasma　Five typical spatial integrated spectra acquired at delay time from 200 ns to 3 μs, as shown in Fig.3, were chosen to show the temporal evolution of the optical emission from the fs-laser ablated plasma. As early as a delay time of 0.2 μs, the spectrum is already dominated by rotational spectra from AlO molecular bands, which shows great difference compared to the case of ns-laser ablation, where the AlO emission appeared at several microseconds after the laser pulse.[18,45] For short delays (e.g. 0.2 μs), the continuum emission contributes about one third in intensity to the total emission. As the delay increases, this emission drops significantly as a result of association of free electrons and ions and reduced bremsstrahlung emission.[46,47]

Spatiotemporal Distribution of Isotopologue Molecules   The plasma plume interacts with ambient air, and the oxygen abundance of materials inside plasma will be modified.   The apparent bandhead intensity ratio of $Al^{18}O$ to $Al^{16}O$ decrease as the decay of plasma, according to the time resolved spectra given in Fig.3. Even at the same delay time, we found that the bandhead height ratios of $Al^{18}O$ to $Al^{16}O$ at different portions of plasma were significantly different (c.f. Fig.4). Six spectra were taken with a same gating time (6 μs) but from different portions of plasma, and were further normalized to 0-1, separately. It clearly shows that the bandhead intensity ratio of $Al^{16}O$ to $Al^{18}O$ drops dramatically as a function of distance from sample surface, and the result implies that the plasma-air chemical reactions are more intense at plasma portions closer to the sample surface.

Before elucidating the reaction pathways or mechanism for the formation of AlO, it is important to study the dynamic distributions of isotopologue molecules and temperature during the evolution of plasma. The chemical reaction rates and stability of products are relevant to temperature.[48] To deduce the temporal evolutions of the number densities of AlO isotopologue molecules, the emission intensities were normalized to the ICCD gate width (in the unit of 1 μs). For example, to obtain the normalized intensity for spectrum acquired with gate width of 2 μs, the measured intensity was then divided by a factor of 2. The temporal profiles of $Al^{16}O$ number density, $Al^{18}O$ number density, $Al^{16}O/Al^{18}O$ number density ratio and temperature as functions of distance from the sample surface are summarized in Fig.5. Notice that the intensities of $Al^{18}O$ and $Al^{16}O$ were deduced from a same spectra thus they are directly comparable. At the delay time of 0.2 μs, both intensities for $Al^{16}O$ and $Al^{18}O$ increase as the increase of distance from sample surface. At later time (>0.3 μs), the profiles feature an intense head located at plasma portion that far away from the sample surface, and the intensities degenerate gradually towards shorter distance from the sample surface. We also remark that the peak intensities of $Al^{16}O$ remain similar at delays of 2 to 6 μs, whilst an apparent degeneration of the peak intensities of $Al^{18}O$ was observed. This difference was obviously revealed by comparing the $Al^{16}O/Al^{18}O$ ratios at different delay times, as shown in Fig.5c. The $Al^{16}O/Al^{18}O$ number density ratios are higher for plasma portion that closer to the sample surface, and decrease as function of distance from sample surface. It is also noticeable that the spatial gradient of the $Al^{16}O/Al^{18}O$ number

density ratio is larger for longer delays (2-6 μs) compared to that of early times (0.2-1.5 μs), and it implies that the chemical reactions for the formation of $Al^{16}O$ is different over plasma decay. The chemical reactions are relevant to the temperature and the temperature profiles are significantly different for early and late stage of plasma, as shown in Fig.5d.

Plasma Chemical Reaction Mechanism for Evolution of $Al^{16}O/Al^{18}O$ Ratio   Several studies have shown that the formation of AlO molecules involves gas-phase combustion of Al with surrounding oxidizers.[18,49,50] A comparison of fs-laser ablation of ^{18}O-enriched Al_2O_3 sample in air and Ar would help to understand the pathways of molecules formation. For the experiments in Ar, a thin Ar flow layer-was applied at the sample surface by placing a flat nozzle (inner size ~1.5 mm) near the laser ablation spot. The vertical propagation characteristic of plasma plume allows the analysis of early time plasma evolution in Ar and late stage of plasma-air chemical reactions when plasma is exposed in air.

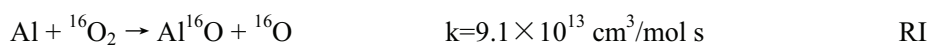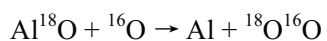As expected, performing this experiment yielded a total different evolutions or profiles of $Al^{16}O/Al^{18}O$ number density ratio, as shown in Fig.6. At early times (0.3-0.5 μs), the plasma plume was exposed in Ar ambient, the Ar layer acts as a barrier that prevents the plasma-air chemical reactions. The experimental results showed that intense AlO emission can still be observed, which implies that association of free Al and O atoms through reaction R1: $Al + O + M \rightarrow AlO + M$ is the dominant pathway of formation of AlO molecules. Moreover, AlO molecules can also be formed through dissociation of laser ablated Al_2O_3 fragments (R2: $Al_2O_3 \rightarrow AlOAlO + O$ and R3: $AlOAlO \rightarrow AlO + AlO$),[51] and possible chemical reaction (R4: $Al + Al_2O_3 \rightarrow 3AlO$).[52] The optimum temperature for the dissociation (R2 and R3) is about 4000 K.[51,53] However, according to the NIST JANAF thermochemical tables,[54] AlO is unstable above 5400 K. Above this temperature, AlO will further dissociate through $AlO \rightarrow Al + O$ shortly after its formation[53], and this agrees well with the results shown in Fig.5. At early time (0.2 μs), AlO molecular spectra were observed, the maximum temperature is lower than 6200 K (c.f. Fig.5d). Moreover, the AlO molecules number density is very low at high temperature zone of plasma (c.f. Fig.5b). It is the primary reason that AlO emission was not observed at early time of ns-laser ablated plasma, in which case the temperature is typically much

higher than 6×10^3 K, as reported by Bai et al.[18] We also remark that direct dissociation of Al_2O_3 particles (R2&R3) and reaction R4 would not be the dominant formation mechanism of AlO for the case of laser ablation in air because the oxygen in Al_2O_3 is ^{18}O-enriched, and reaction R2, R3 and R4 would lead to an increase of $Al^{18}O/Al^{16}O$ ratio, which is inconsistent to experimental results shown in Fig.5c.
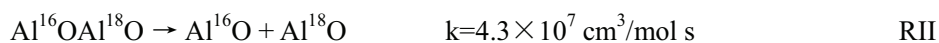
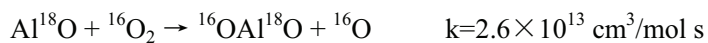Despite the absolute $Al^{16}O/Al^{18}O$ ratio difference, the ratio profiles at early time are significantly different. The $Al^{16}O/Al^{18}O$ ratio *vs* distance from sample surface profile is nearly flat in Ar ambient, whereas the $Al^{16}O/Al^{18}O$ ratio decreases as the increase of distance from the sample surface in air (c.f. Fig.5c and Fig.6). It implies that oxygen molecules from air trend to diffuse into plasma at plasma portions closer to the sample surface. We also remark that the tested $Al^{16}O/Al^{18}O$ number density ratios at delay of 0.3-0.5 μs in Ar are close to 0.44 (70 atom % ^{18}O), whereas the ratios are over 0.9 in case of laser ablation in air. This is not surprising because air molecules near the laser sampling spot can be directly dissociated by the extreme intense focused fs-laser.[55] Moreover, the air oxygen molecules can also dissociates through inelastic electron-molecule collision.[56] Both processes enrich the ^{16}O abundance of initial plasma materials. Al can also directly react with oxygen molecules that diffused into plasma via reactions: R5 $Al + {}^{16}O_2 \rightarrow Al^{16}O + {}^{16}O$ and R6 $AlO + {}^{16}O_2 \rightarrow Al^{16}OO + {}^{16}O$. $Al^{16}OO$ can further dissociate through reaction R7 $Al^{16}OO \rightarrow Al^{16}O + O$ or $Al^{16}OO \rightarrow AlO + {}^{16}O$. Both reactions R5 and R6 promote the formation of $Al^{16}O$, and lead to enrichment of ^{16}O neutrals inside plasma plume. More $Al^{16}O$ can form through reaction R1. This is consistent with the experimental observations that the number density ratio of $Al^{16}O/Al^{18}O$ increase over time for early time plasma.

The plasma temperature after 0.5 μs is around 3500 K. The concentrations of neutrals Al, O and AlO were roughly estimated with chemical reaction equilibrium theory, assuming that plasma is in local thermodynamics equilibrium condition. Standard Gibbs free energy $\Delta_f G°$ of reactions R1 and R5 were -107.7 and -66.6 kJ/mol, respectively. These values were derived from standard free energies of formation given in the NIST-JANAF.[54] The equilibrium constants K_{eq} is related to $\Delta_f G°$ by $K_{eq} = \exp(-\Delta_f G°/RT)$ and partial pressure of species is related to K_{eq} by

$K_{eq} = \Pi_{products} p_i^{n_i} / \Pi_{reactants} p_j^{n_j}$, where p_i is the partial pressure of species i, n_i is the power of

the coefficient in the equation for the reaction, R is gas constant and T is temperature. Using the

equilibrium expressions for reactions R1 and R5 at 3500 K, we have

$P_{AlO}/P_{Al}P_O = 40.5$ and $P_{AlO}P_O/P_{Al}P_{O_2} = 9.9$. The ratio of each species such as neutral Al and O

atoms and AlO radicals can be further calculated, and the result reveals that about 98% of Al exists in

form of AlO. The calculation suggests that the concentration of AlO radicals is significant higher than

that of neutral Al atoms, and most of neutral Al atoms have already depleted at the later time. Thus,

combustion of neutral Al with surrounding oxygen molecules from air (R5-R7) is not the dominate

mechanism for the increment of $Al^{16}O/Al^{18}O$ ratio, especially for late stage plasma over 3 μs, during

which the density of neutral Al atoms is very low, and significant number density decay of both $Al^{16}O$

and $Al^{18}O$ was observed. Performing temporal analysis of spatially integrated spectra of laser ablated

plasma in air yields that the $Al^{18}O$ number density reaches its maximum around 1.5 μs, whereas the

$Al^{16}O$ number density reaches its maximum at 3 μs. The spatial integrated number density ratio of

$Al^{16}O/Al^{18}O$ is linearly related to delay time with $R^2 > 0.999$ in 2-10 μs (c.f. inset of Fig.5c). The

$Al^{16}O/Al^{18}O$ ratio at 10 μs is about 2 times of that at 2 μs. The mechanism for increase of spatial

integrated number density ratio of $Al^{16}O/Al^{18}O$ over time can attributed to the oxygen isotope

exchange effect ($Al^{18}O \rightarrow Al^{16}O$) during the dynamic equilibrium of forward and backward chemical

reaction through route:

$Al^{18}O + {}^{16}O \rightarrow Al + {}^{18}O^{16}O$

$Al + {}^{16}O_2 \rightarrow Al^{16}O + {}^{16}O$ k=9.1×10^{13} cm^3/mol s   RI

and routes

$Al^{18}O + {}^{16}O_2 \rightarrow {}^{16}OAl^{18}O + {}^{16}O$ k=2.6×10^{13} cm^3/mol s

${}^{16}OAl^{18}O \rightarrow Al^{16}O + {}^{18}O$ k=2.9×10^9 cm^3/mol s

${}^{16}OAl^{18}O + Al \rightarrow Al^{16}OAl^{18}O$ k=5.0×10^5 cm^3/mol s

$Al^{16}OAl^{18}O \rightarrow Al^{16}O + Al^{18}O$ k=4.3×10^7 cm^3/mol s   RII

where k is reaction rate coefficient have been calculated at temperature 3500 K with parameters

reported by Huang $et\ al.$[57] Route RI is thought to be the dominate mechanism for the oxygen isotope

exchange because route RI is one step reaction with fast reaction rate and route RII consists multi-step reactions with much lower reaction rates. In fact, the standard enthalpy (ΔH) for reactions in route RI is close to zero because the dissociation energies of AlO and O_2 are very similar. The reaction has a near-zero barrier.[48] Evidently, oxygen atoms in $Al^{18}O$ molecules can be easily replaced by ^{16}O from ambient air molecules, which favors rapid oxygen isotope exchange ($Al^{18}O \rightarrow Al^{16}O$) as observed in experiment.

CONCLUSIONS

We present the latest scientific finding on the formation of isotopologue molecules ($Al^{16}O$ and $Al^{18}O$) in fs-laser induced plasma from ^{18}O-enriched Al_2O_3 pellet with LAMIS technique. The plasma imaging study shows that propagation in one direction normal to the sample surface dominants the evolution of fs-laser ablated plume, whereas the plume maintained similar radial size. Laser ablated sample materials and laser dissociated air molecules near sampling spot constitute the initial composition of plasma, and oxygen abundance of plasma can be modified in terms of collision excitation of air oxygen molecules and combusting of Al species during the evolution of plasma. The spatiotemporal distributions of $Al^{16}O$ and $Al^{18}O$ molecules were measured through fitting multi-vibrational $\Delta v = -1$ bands of AlO $B\ ^2\Sigma^+ \rightarrow X\ ^2\Sigma^+$ system with using synthetic spectra, and the $Al^{16}O/Al^{18}O$ number density ratio was found to be significantly dependent on time after the laser pulse and distance above the sample surface. The incomplete dissociation of specific bonds in the original molecular structure was shown to be an ignorable mechanism for the formation of AlO. Chemical reactions between plasma materials and ambient oxygen was shown to be a dominate mechanism for the formation of AlO, and oxygen isotope exchange effect acts as a complementary mechanism for the evaluation of $Al^{16}O/Al^{18}O$ number density ratio for late plasma (about 2-10 µs). The results also reveals that the formation mechanism of AlO is significantly differ to that of C_2 in laser induced plasma from organic compounds, in which case, direct release C_2 in the original molecular structure was proven to be an important mechanism.[23,24]

AUTHOR INFORMATION

Corresponding Author

*E-mail: X_Mao@lbl.gov

REFERENCES

(1)   Maurice, S.; Wiens, R. C.; Saccoccio, M.; Barraclough, Gasnault, O.;·Forni O.;·Mangold N.;·Baratoux D.;·Bender S.;·Berger G.·*et al*. *Space Sci. Rev.* **2012**, *170*, 95–166.

(2)   Meslin, P.-Y.; Gasnault, O.; Forni, O.; Schroder, S., Cousin, A.; Berger, G.; Clegg, S.M., Lasue, J.; Maurice, A.; Sautter, V. *et al*. *Science* **2013**, *341*, 1238670.

(3)   Sautter, V.; Toplis, M. J.; Wiens, R. C.; Cousin, A.; Fabre, C.; Gasnault, O.; Maurice, S.; Forni, O.; Lasue, J.; Ollila, A. *et al*. *Nat. Geosci.* **2015**, *8*, 605–609.

(4)   Fortes, F. J.; Moros, J.; Lucena, P.; Cabalín, L. M.; Laserna, J. J. *Anal. Chem.* **2013**, *85*, 640–669.

(5)   Russo, R. E.; Mao, X.; Gonzalez, J. J.; Zorba, V.; Yoo, J. *Anal. Chem.* **2013**, *85*, 6162–6177.

(6)   Rao, E. N.; Sunku, S.; Venugopal Rao, S. *Appl. Spectrosc.* **2015**, *69*, 1342–1354.

(7)   Serrano, J.; Moros, J.; Sánchez, C.; Macías, J.; Laserna, J. J. *Anal. Chim. Acta.* **2014**, *806*, 107–116.

(8)   Moros, J.; Serrano, J.; Gallego, F. J.; Macías, J.; Laserna, J. J. *Talanta* **2013**, *110*, 108–117.

(9)   Gaona, I.; Serrano, J.; Moros, J.; Laserna, J. J. *Anal. Chem.* **2014**, *86*, 5045–5052.

(10)   Gaft, M.; Nagli, L.; Eliezer, N.; Groisman, Y.; Forni, O. *Spectrochim. Acta Part B* **2014**, *98*, 39–47.

(11)   Sarkar, A.; Mao, X.; Russo, R. E. *Spectrochim. Acta Part B* **2014**, *92*, 42–50.

(12)   Russo, R. E.; Bol'shakov, A.; Mao, X.; McKay, C. P.; Perry, D. L.; Sorkhabi, O. *Spectrochim. Acta Part B* **2011**, *66*, 99–104.

(13)   Bol'shakov, A. A.; Mao, X.; González, J. J.; Russo, R. E. *J. Anal. At. Spectrom.* **2016**, *113*, 106–112.

(14)   Bol′shakov, A. A.; Mao, X.; Jain, J.; McIntyre, D. L.; Russo, R. E. *Spectrochim. Acta Part B* **2015**, *113*, 106–112.

(15)   Sarkar, A.; Mao, X.; Chan, G. C. Y.; Russo, R. E. *Spectrochim. Acta Part B* **2013**, *88*, 46–53.

(16)   Hou, H.; Chan, G. C.-Y.; Mao, X.; Zorba, V.; Zheng, R.; Russo, R. E. *Anal. Chem.* **2015**, *87*, 4788–4796.

(17)   Serrano, J.; Moros, J.; Laserna, J. J. *Anal. Chem.* **2015**, *87*, 2794–2801.

(18)   Bai, X.; Motto-Ros, V.; Lei, W.; Zheng, L.; Yu, J. *Spectrochim. Acta Part B* **2014**, *99*, 193–200.

(19)   Harilal, S. S.; Brumfield, B. E.; Cannon, B. D.; Phillips, M. C. *Anal. Chem.* **2016**, *88*, 2296–2302.

(20)   Grégoire, S.; Boudinet, M.; Pelascini, F.; Surma, F.; Detalle, V.; Holl, Y. *Anal. Bioanal. Chem.* **2011**, *400*, 3331–3340.

(21)   Grégoire, S.; Motto-Ros, V.; Ma, Q. L.; Lei, W. Q.; Wang, X. C.; Pelascini, F.; Surma, F.; Detalle, V.; Yu, J. *Spectrochim. Acta Part B* **2012**, *74–75*, 31–37.

(22)   St-Onge, L.; Sing, R.; Béchard, S.; Sabsabi, M. *Appl. Phys. A Mater. Sci. Process.* **1999**, *69*, S913.

(23)   Dong, M.; Chan, G. C.-Y.; Mao, X.; Gonzalez, J. J.; Lu, J.; Russo, R. E. *Spectrochim. Acta Part B* **2014**, *100*, 62–69.

(24)   Glaus, R.; Riedel, J.; Gornushkin, I. *Anal. Chem.* **2015**, *87*, 10131–10137.

(25)   Serrano, J.; Moros, J.; Laserna, J. J. *J. Anal. At. Spectrom.* **2015**, *30*, 2343–2352.

(26)   Hou, H.; Chan, G. C.-Y.; Mao, X.; Zheng, R.; Zorba, V.; Russo, R. E. *Spectrochim. Acta Part B* **2015**, *113*, 113–118.

(27)   Mao, X.; Bol'shakov, A.; Choi, I.; McKay, C. P.; Perry, D. L.; Sorkhabi, O.; Russo, R. E. *Spectrochim. Acta Part B* **2011**, *66*, 767–775.

(28)   Sriramachandran, P.; Viswanathan, B.; Shanmugavel, R. *Sol. Phys.* **2013**, *286*, 315–326.

(29)   Tenenbaum, E. D.; Ziurys, L. M. *Astrophys. J.* **2009**, *694*, L59–L63.

(30)   Parigger, C. G.; Hornkohl, J. O. *Spectrochim. Acta Part A Mol. Biomol. Spectrosc.* **2011**, *81*, 404–411.

(31)   Surmick, D. M.; Parigger, C. G. *Appl. Spectrosc.* **2015**, *68*, 992–996.

(32)   Hermann, J.; Lorusso, A.; Perrone, A.; Strafella, F.; Dutouquet, C.; Torralba, B. *Phys. Rev. E* **2015**, *92*, 53103.

(33)   Parigger, C. G.; Woods, A. C.; Surmick, D. M.; Gautam, G.; Witte, M. J.; Hornkohl, J. O. *Spectrochim. Acta Part B* **2015**, *107*, 132–138.

(34)   Serrano, J.; Moros, J.; Javier Laserna, J. *Phys. Chem. Chem. Phys.* **2016**, *18*, 2398–2408.

(35)   Sreedhar, S.; Nageswara Rao, E.; Manoj Kumar, G.; Tewari, S. P.; Venugopal Rao, S. *Spectrochim. Acta Part B* **2013**, *87*, 121–129.

(36)   Dikmelik, Y.; McEnnis, C.; Spicer, J. B. *Opt. Express* **2008**, *16*, 5332–5337.

(37)   Baudelet, M.; Guyon, L.; Yu, J.; Wolf, J.-P.; Amodeo, T.; Fréjafon, E.; Laloi, P. *J. Appl. Phys.* **2006**, *99*, 84701.

(38)   Sunku, S.; Gundawar, M. K.; Myakalwar, A. K.; Kiran, P. P.; Tewari, S. P.; Rao, S. V. *Spectrochim. Acta Part B* **2013**, *79–80*, 31–38.

(39)   Freeman, R. J.; Harilal, S. S.; Diwakar, K. P.; Verhoff, B.; Hassanein, A. *Spectrochim. Acta Part B* **2013**, *87*, 43–50.

(40)   Gurevich, E. L.; Hergenröder, R. *Appl. Spectrosc.* **2007**, *61*, 233A–242A.

(41)   Liu, W.; Chin, S. *Opt. Express* **2005**, *13*, 5750–5755.

(42)   Ryabtsev, A.; Pouya, S.; Koochesfahani, M.; Dantus, M. *Opt. Express* **2014**, *22*, 26098–26102.

(43)   Dong, M.; Mao, X.; Gonzalez, J. J.; Lu, J.; Russo, R. E. *Anal. Chem.* **2013**, *85*, 2899–2906.

(44)   Patrascu, A. T.; Yurchenko, S. N.; Tennyson, J. *Mon. Not. R. Astron. Soc.* **2015**, *449*, 3613–3619.

(45)   Lam, J.; Motto-ros, V.; Misiak, D.; Dujardin, C.; Ledoux, G.; Amans, D.; Cnrs, U. M. R.; Matière,

I. L. *Spectrochim. Acta Part B* **2014**, *101*, 86–92.

(46)   De Giacomo, A.; Gaudiuso, R.; Dell'Aglio, M.; Santagata, A. *Spectrochim. Acta Part B* **2010**, *65*, 385–394.

(47)   De Giacomo, A.; Dell'Aglio, M.; De Pascale, O.; Gaudiuso, R.; Palleschi, V.; Parigger, C.; Woods, A. *Spectrochim. Acta Part B* **2014**, *100*, 180–188.

(48)   Politzer, P.; Lane, P.; Grice, M. E. *J. Phys. Chem. A* **2001**, *105*, 7473–7480.

(49)   Peuker, J. M.; Lynch, P.; Krier, H.; Glumac, N. *Propellants, Explos. Pyrotech.* **2013**, *38*, 577–585.

(50)   Badiola, C.; Gill, R. J.; Dreizin, E. L. *Combust. Flame* **2011**, *158*, 2064–2070.

(51)   Brewer, L.; Searcy, A. W. *J. Am. Chem. Soc.* **1951**, *73*, 5308–5314.

(52)   Hoch, M.; Johnston, H. L. *J. Am. Chem. Soc.* **1954**, *76*, 2560–2561.

(53)   Rains, R. K.; Kadlec, R. H. *Metall. Trans.* **1970**, *1*, 1501–1506.

(54)   NIST-JANAF Thermochemical Tables http://kinetics.nist.gov/janaf. (Accessed May 1, 2016)

(55)   Cornaggia, C.; Lavancier, J.; Normand, D.; Morellec, J.; Agostini, P.; Chambaret, J. P.; Antonetti, a. *Phys. Rev. A* **1991**, *44*, 4499–4505.

(56)   Itikawa, Y.; Ichimura, A.; Onda, K.; Sakimoto, K.; Takayanagi, K.; Hatano, Y.; Hayashi, M.; Nishimura, H.; Tsurubuchi, S. *J. Phys. Chem. Ref. Data* **1989**, *18*, 23–42.

(57)   Huang, Y.; Risha, G. a.; Yang, V.; Yetter, R. a. *Combust. Flame* **2009**, *156*, 5–13.

Figure Captions

Fig. 1 AlO emission images of fs-laser ablated plasmas from ^{18}O-enriched Al_2O_3 pellets. Images (a-h) were captured at different delay times as labeled at bottom of each image. For recording these images, narrow bandpass filters with transmission centered at 488 nm (AlO Δv=0 bands) were used. Each image was an average of 20 laser shots and was normalized to its maximum intensity.
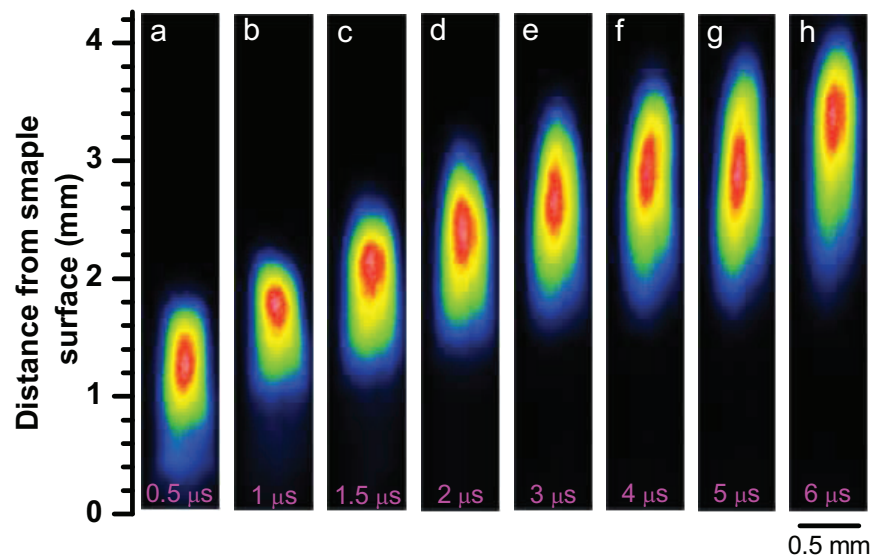
Fig.2 Typical LAMIS spectrum acquired from the $Al^{18}O$-enriched Al_2O_3 pellet and its fitting. The molecular bands ($\Delta v = 0,-1$) were re-constructed through fitting procedure. The intensity scale expanded inset (bottom) emphasizes the rotational tails of $\Delta v = 0$ bands of both $Al^{16}O$ and $Al^{18}O$. Experimental spectrum was acquired with a 2 μs gate delay, 1 μs gate width and at distance from sample surface of 2.89 mm.

Fig.3 Comparison of experimental (black symbols) and simulated spectra (red lines) for AlO B → X ($\Delta v = -1$) bands. The spectra were spatially integrated. GD: gate delay, GW: gate width, Res: relative residual.
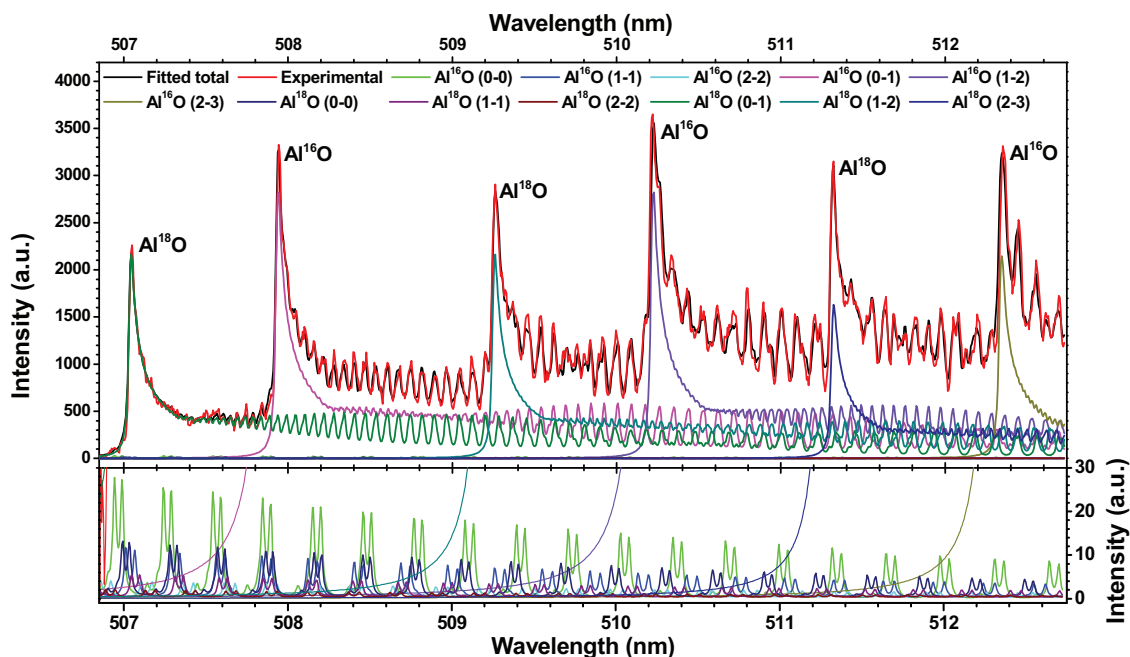
Fig.4 Part of emission B → X (0-1) of $Al^{18}O$ and $Al^{16}O$ formed during fs-laser ablation of ^{18}O-enriched Al_2O_3 pellet. Spectra were acquired with a 6 μs gate delay, 2 μs gate width, and were averaged over 100 laser pulses. Each spectrum was normalized to 0-1. The inset shows the bandhead intensity ratio of $Al^{16}O$ to $Al^{18}O$ versus distance from sample surface.

Fig.5 Spatial profiles of predicted $Al^{16}O$ number density (a), $Al^{18}O$ number density (b), $Al^{16}O/Al^{18}O$ number density ratios (c) and rotational temperature (d) at different delay times. Data with hollow and solid symbols represent the relative fitting residuals are over and below 2×10^{-3}, respectively. The inset in subfigure c shows the evolution of $Al^{16}O/Al^{18}O$ number density ratio as a function of delay time, and each data point was obtained by fitting the spatial integrated spectrum.

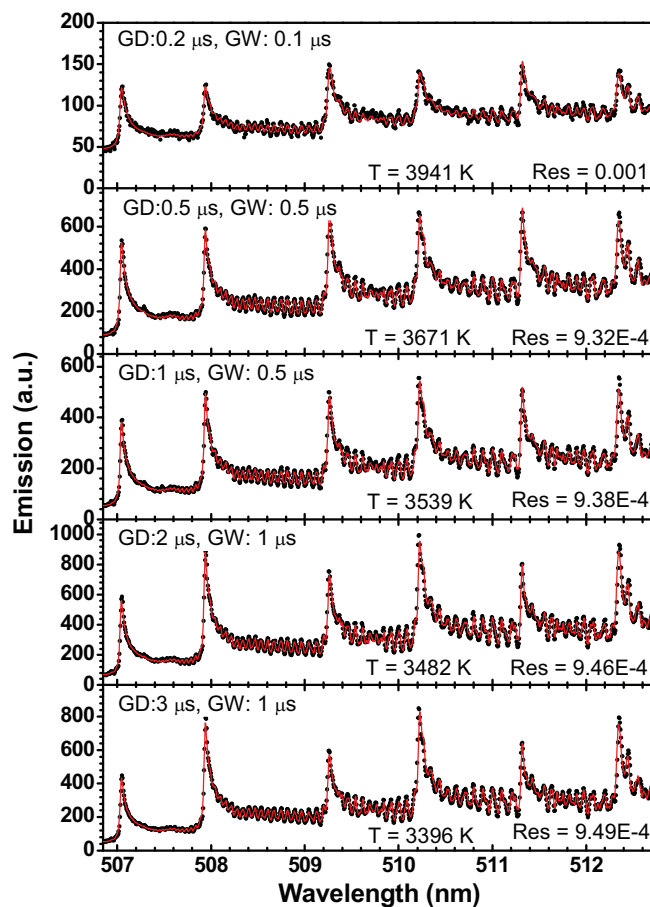**Fig.6** Spatial profiles of predicted $Al^{16}O/Al^{18}O$ number density ratios at different delay times. Data with hollow and solid symbols represent the relative fitting residuals are over and below 2×10^{-3}, respectively. A thin Ar flow layer (about 1.5 mm) was created at the surface of sample during fs-laser ablation.
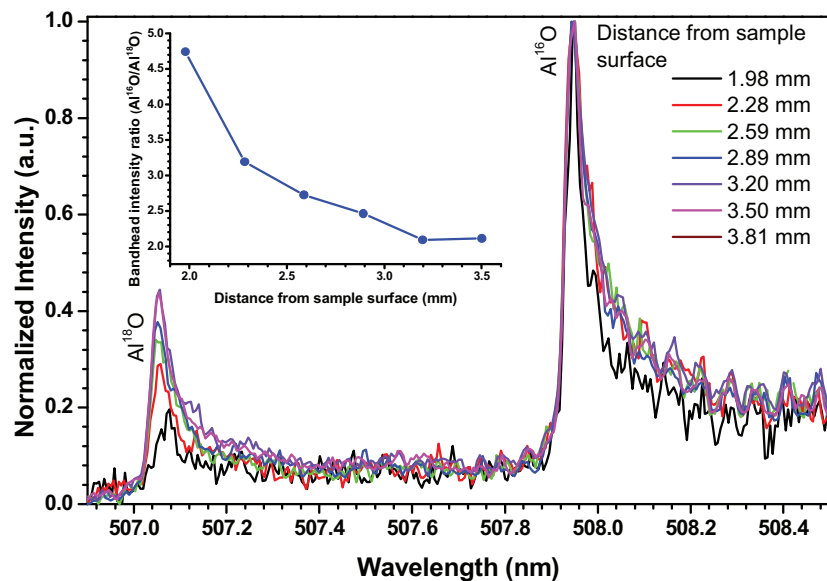
Fig. 1 AlO emission images of fs-laser ablated plasmas from ^{18}O-enriched Al_2O_3 pellets. Images (a-h) were captured at different delay times as labeled at bottom of each image. For recording these images, narrow bandpass filters with transmission centered at 488 nm (AlO Δv=0 bands) were used. Each image was an average of 20 laser shots and was normalized to its maximum intensity.
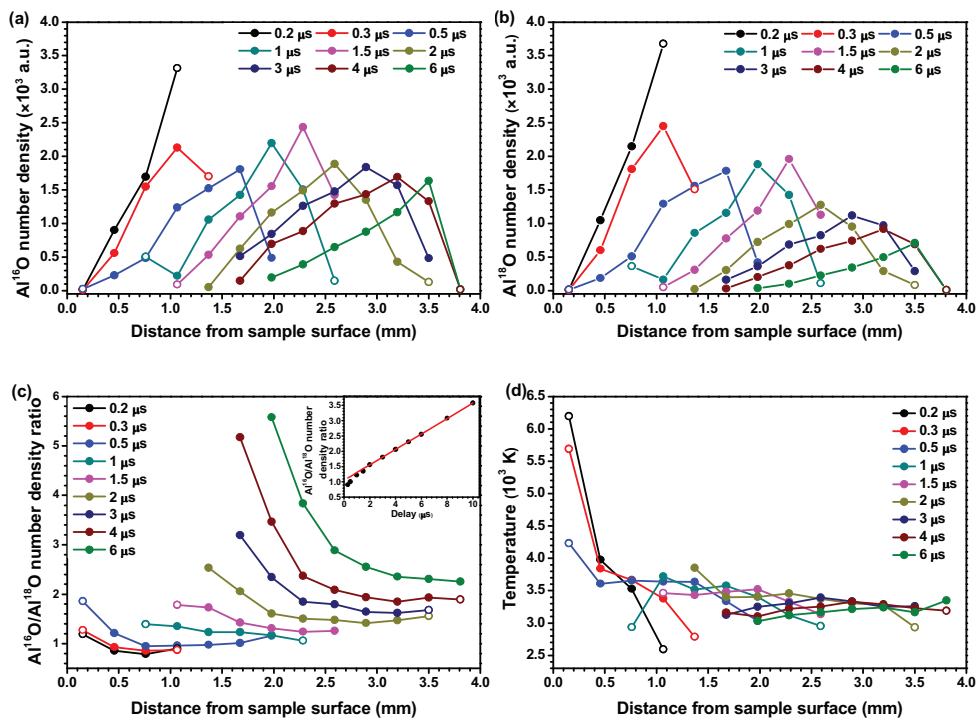
Fig.2 Typical LAMIS spectrum acquired from the $Al^{18}O$-enriched Al_2O_3 pellet and its fitting. The molecular bands ($\Delta v = 0,-1$) were re-constructed through fitting procedure. The intensity scale expanded inset (bottom) emphasizes the rotational tails of $\Delta v = 0$ bands of both $Al^{16}O$ and $Al^{18}O$. Experimental spectrum was acquired with a 2 µs gate delay, 1 µs gate width and at distance from sample surface of 2.89 mm.
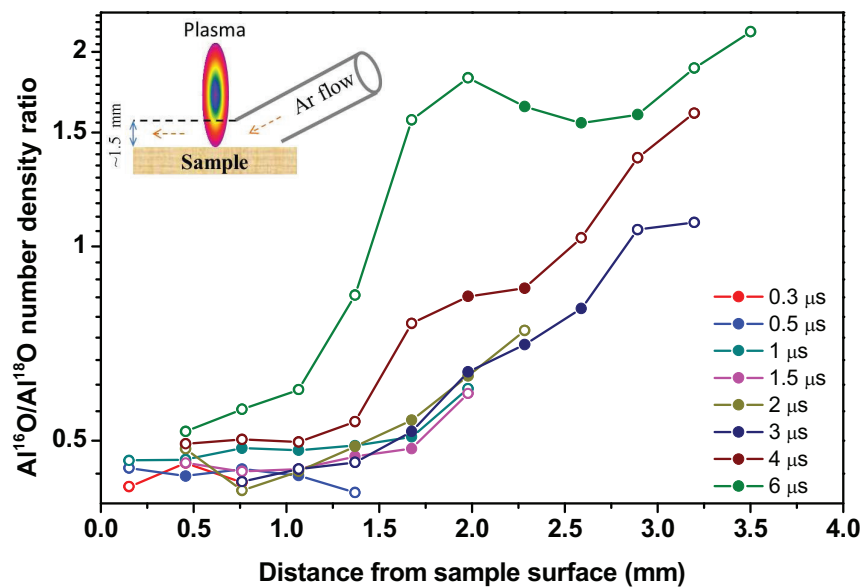
Fig.3 Comparison of experimental (black symbols) and simulated spectra (red lines) for AlO B → X (Δv = -1) bands. The spectra were spatially integrated. GD: gate delay, GW: gate width, Res: relative residual.

Fig.4 Part of emission B → X (0-1) of Al^{18}O and Al^{16}O formed during fs-laser ablation of ^{18}O-enriched Al$_2$O$_3$ pellet. Spectra were acquired with a 6 µs gate delay, 2 µs gate width, and were averaged over 100 laser pulses. Each spectrum was normalized to 0-1. The inset shows the bandhead intensity ratio of Al^{16}O to Al^{18}O versus distance from sample surface.

Fig.5 Spatial profiles of predicted Al^{16}O number density (a), Al^{18}O number density (b), Al^{16}O/Al^{18}O number density ratios (c) and rotational temperature (d) at different delay times. Data with hollow and solid symbols represent the relative fitting residuals are over and below 2×10^{-3}, respectively. The inset in subfigure c shows the evolution of Al^{16}O/Al^{18}O number density ratio as a function of delay time, and each data point was obtained by fitting the spatial integrated spectrum.

Fig.6 Spatial profiles of predicted $Al^{16}O/Al^{18}O$ number density ratios at different delay times. Data with hollow and solid symbols represent the relative fitting residuals are over and below 2×10^{-3}, respectively. A thin Ar flow layer (about 1.5 mm) was created at the surface of sample during fs-laser ablation.

TOC graphic